

Article

Angular Position Sensor Based on Anisotropic Magneto-resistive and Anomalous Nernst Effect

Jiaqi Wang ^{1,†} , Hang Xie ^{1,†}  and Yihong Wu ^{1,2,*}

¹ Department of Electrical and Computer Engineering, National University of Singapore, Singapore 117583, Singapore

² National University of Singapore (Chong Qing) Research Institute, Chongqing Liang Jiang New Area, Chongqing 401123, China

* Correspondence: elewuyh@nus.edu.sg

† These authors contributed equally to this work.

Abstract: Magnetic position sensors have extensive applications in various industrial sectors and consumer products. However, measuring angles in the full range of 0–360° in a wide field range using a single magnetic sensor remains a challenge. Here, we propose a magnetic position sensor based on a single Wheatstone bridge structure made from a single ferromagnetic layer. By measuring the anisotropic magnetoresistance (AMR) signals from the bridge and two sets of anomalous Nernst effect (ANE) signals from the transverse ports on two perpendicular Wheatstone bridge arms concurrently, we show that it is possible to achieve 0–360° angle detection using a single bridge sensor. The combined use of AMR and ANE signals allows a mean angle error in the range of 0.51–1.05° within a field range of 100 Oe–10,000 Oe to be achieved.

Keywords: magnetic position sensor; anisotropic magnetoresistance; anomalous Nernst effect; harmonic measurement



Citation: Wang, J.; Xie, H.; Wu, Y. Angular Position Sensor Based on Anisotropic Magneto-resistive and Anomalous Nernst Effect. *Sensors* **2024**, *24*, 1011. <https://doi.org/10.3390/s24031011>

Academic Editors: Nerija Žurauskienė and Voitech Stankevič

Received: 10 January 2024

Revised: 30 January 2024

Accepted: 1 February 2024

Published: 4 February 2024



Copyright: © 2024 by the authors. Licensee MDPI, Basel, Switzerland. This article is an open access article distributed under the terms and conditions of the Creative Commons Attribution (CC BY) license (<https://creativecommons.org/licenses/by/4.0/>).

1. Introduction

Precise measurements of angular positions are indispensable across diverse domains, including manufacturing, space exploration, the internet of things (IoT), medical technology, consumer products, navigation, and industrial automation [1–7]. Commercial magnetic angle sensing devices typically employ Hall effect [8], anisotropic magnetoresistance (AMR) [9], giant magnetoresistance (GMR) [10], and tunnel magnetoresistance (TMR) sensors [11]. To achieve full 360° detection, it is common to employ two orthogonally positioned Hall effect, GMR, or TMR sensors to obtain the sine and cosine signals from which the angle position can be derived using an arctangent function. Although AMR sensors typically offer superior signal-to-noise ratio and high accuracy compared to Hall effect, GMR, and TMR sensors, two AMR sensors can only detect the angle in the range of 0–180°, and an additional sensor is required to achieve full 360° detection [12,13]. This would increase the complexity of the sensor design and manufacturing cost. Furthermore, the GMR and TMR sensors have a limited dynamic range (usually less than 1000 Oe), which imposes limitations in some practical applications that require a large field range.

Recently, several angular position sensors based on emerging physical phenomena such as spin Hall magnetoresistance (SMR) and spin-orbit torque (SOT) have been demonstrated. These sensors typically have a much simpler design as compared to the conventional AMR, GMR, and TMR sensors. In fact, all of these sensors, including the SMR sensor [14], spin torque gate (STG) sensor [15], SOT-enabled anomalous Hall (AHE) vector magnetometer [16], and SOT-based magnetic angular sensor [17] are based merely on a simple ultrathin ferromagnet (FM)/heavy metal (HM) bilayer without any magnetic bias, which greatly simplifies the sensor design and reduces the manufacturing cost. However, the SOT-based sensors typically have a relatively small dynamic range, which may limit

their applications in settings with a large environmental magnetic field. Alternatively, unidirectional magnetoresistance (UMR) can also be explored for 0–360° angle detection [18], but it faces significant challenges and limitations due to the substantial noise in the UMR signals, which adversely impacts the performance and accuracy of the sensor. Here, we propose an extremely simple angular position sensor based on the AMR and anomalous Nernst effect (ANE) in a single ferromagnetic (FM) layer, which allows for 0–360° angle detection using a single Wheatstone bridge. Compared to the UMR signals, the ANE signals exhibit low noise and nearly zero offset and, importantly, they are readily accessible in almost all conductive ferromagnetic films, provided there is a vertical temperature gradient. The latter is conveniently achieved through the sensing current. We demonstrate experimentally that, by simultaneously measuring the first harmonic longitudinal and second harmonic transverse voltages of a CoFeB-based bridge device under an AC sensing current, it is possible to detect angles within 0–360° at a mean angle error of 0.51–1.05° with a dynamic field range of 100 Oe–10,000 Oe.

2. Experimental Details

A stack consisting of CoFeB (3, 6, 10, 15 nm)/MgO (2 nm)/Ta (1.5 nm) from bottom to top is deposited on the Si/SiO₂ substrate by magnetron sputtering with a base pressure of 2×10^{-8} Torr and a working pressure of 3×10^{-3} Torr. The Microtech LaserWriter system, equipped with a 405 nm laser, is employed for patterning the device into a Wheatstone bridge. Each Wheatstone bridge arm has dimensions of $30 \mu\text{m} \times 200 \mu\text{m}$. Following the deposition of the film stack and patterning of the device, electrodes and contact pads consisting of Ta (5 nm)/Cu (100 nm)/Pt (10 nm) are formed on the four terminals of the bridge for electrical transport measurements. Finally, the devices are thermally annealed at 250 °C for 1 h in a vacuum furnace with a pressure of less than 1×10^{-5} Torr. For electrical measurements, we use a Keithley 6221 current source to supply an AC current to two diagonal terminals of the bridge, and an MFLI lock-in amplifier from Zurich Instruments is used to measure both the first harmonic bridge output and second harmonic Hall voltage signals from the two adjacent arms. All the electrical measurements are performed in a Quantum Design Versalab PPMS system with angle rotator.

3. Results

3.1. Derivation of the First and Second Harmonic Signals

Figure 1a,b show the layer structure of the sensor and schematic of the measurement setup, respectively, where $\vec{H}_{\text{ext}} = H_{\text{ext}}(\sin \theta_H \cos \varphi_H, \sin \theta_H \sin \varphi_H, \cos \theta_H)$ is an in-plane external field with azimuthal angle φ_H and polar angle θ_H ($\theta_H = 90^\circ$ in the present case). At large H_{ext} , the magnetization (\vec{M}) of the FM layer will be aligned with that of the external field, and therefore, its direction is: $\hat{m} = \frac{\vec{M}}{|\vec{M}|} = (\sin \theta_H \cos \varphi_H, \sin \theta_H \sin \varphi_H, \cos \theta_H)$. When a charge current (I) flows through the bridge arms consisting of CoFeB, a temperature gradient ∇T will be established in the film thickness direction (i.e., z -direction) due to the difference in thermal conductivity between air and the substrate [19], as shown in Figure 1a. The magnitude of ∇T is proportional to the power dissipation, i.e., $|\nabla T| \propto I^2 R$, where R is the resistance of the device [20]. This in turn will induce a transverse voltage signal in the respective arms due to the ANE in CoFeB. Phenomenologically, the ANE-induced electric field can be written as $\vec{E} = \frac{S_{\text{ANE}}}{|\vec{M}|} \vec{M} \times \nabla T$, where S_{ANE} is the anomalous Nernst effect coefficient, indicating the strength and sign of the ANE for a particular material [21].

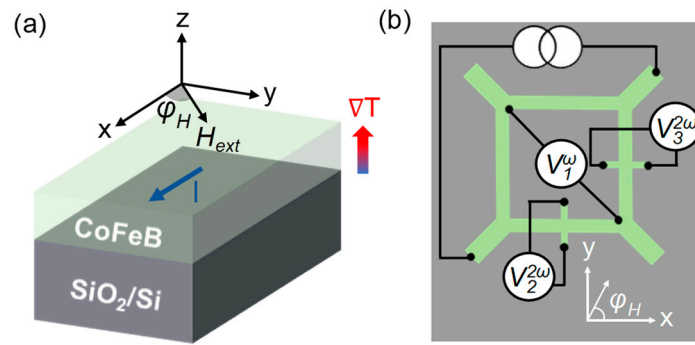


Figure 1. (a) Illustration of the layer structure of the angle sensing device; (b) Schematic of the harmonic measurement setup.

Without loss of generality, the total electric field (\vec{E}) in the FM layer can be expressed in a generalized Ohm's law as follows [20,22]:

$$\vec{E} = \rho_0 \vec{J} + \frac{\Delta\rho_{\text{OMR}}}{|\vec{H}_{\text{ext}}|^2} \left(\vec{J} \cdot \vec{H}_{\text{ext}} \right) \vec{H}_{\text{ext}} + \frac{\Delta\rho_{\text{AMR}}}{|\vec{M}|^2} \left(\vec{J} \cdot \vec{M} \right) \vec{M} - \frac{\rho_{\text{OHE}}}{|\vec{H}_{\text{ext}}|} \vec{J} \times \vec{H}_{\text{ext}} - \frac{\rho_{\text{AHE}}}{|\vec{M}|} \vec{J} \times \vec{M} + \frac{S_{\text{ANE}}}{|\vec{M}|} \vec{M} \times \nabla T, \quad (1)$$

where ρ_0 is the longitudinal resistivity, \vec{J} is the current density. $\Delta\rho_{\text{OMR}}$, $\Delta\rho_{\text{AMR}}$, ρ_{OHE} , and ρ_{AHE} denote the resistivity changes due to the ordinary magnetoresistance (OMR), AMR, ordinary Hall effect (OHE) and AHE, respectively. The sixth term is the contribution from the ANE. As mentioned above, ∇T can be expressed as: $\nabla T = KI^2(0, 0, 1)$, where K is a device-specific coefficient, indicating a proportional relationship between $|\nabla T|$ and I^2 . As shown in Figure 1b, three voltage signals, namely V_1^ω , $V_2^{2\omega}$, and $V_3^{2\omega}$, were acquired simultaneously with an AC current ($I = I_0 \sin \omega t$) applied to the two current terminals. V_1^ω is the first harmonic signal induced by the AMR effect, whereas $V_2^{2\omega}$ and $V_3^{2\omega}$ are the second harmonic signals caused by the ANE in the two adjacent arms, named arm-x and arm-y, respectively. The longitudinal resistance of arm-x and arm-y can be expressed as $R_0 = \frac{L\rho_0}{A}$, where A and L are the cross-sectional area and length of the arm, respectively. The current density in the two arms can be expressed as $\vec{J}_x = \frac{I_0 \sin \omega t}{2A} (1, 0, 0)$, $\vec{J}_y = \frac{I_0 \sin \omega t}{2A} (0, 1, 0)$, respectively. By substituting the expressions of ∇T , \vec{H}_{ext} , \vec{J}_x , and \hat{m} into Equation (1), the longitudinal voltage of arm-x ($V_{\text{arm-x}}$) can be expressed as:

$$V_{\text{arm-x}} = L\vec{E} \cdot \hat{x} = \left(\frac{L\rho_0 I_0}{2A} + \frac{L\Delta\rho_{\text{OMR}} I_0}{2A} \sin^2 \theta_H \frac{1+\cos 2\varphi_H}{2} + \frac{L\Delta\rho_{\text{AMR}} I_0}{2A} \sin^2 \theta_H \frac{1+\cos 2\varphi_H}{2} \right) \sin \omega t + \frac{1}{4} L S_{\text{ANE}} K I_0^2 \sin \theta_H \sin \varphi_H \sin^2 \omega t, \quad (2)$$

where \hat{x} is a unit vector along x -axis. After neglecting the effect of OMR, and substituting $\theta_H = 90^\circ$ into Equation (2), the first harmonic component of $V_{\text{arm-x}}$ is:

$$V_{\text{arm-x}}^\omega = \frac{R'_0 I_0}{2} + \frac{R_{\text{AMR}}}{4} I_0 \cos 2\varphi_H, \quad (3)$$

where $R'_0 = R_0 + \frac{R_{\text{AMR}}}{2}$ and $R_{\text{AMR}} = \frac{L\Delta\rho_{\text{AMR}}}{A}$. The corresponding first harmonic resistance of arm-x ($R_{\text{arm-x}}^\omega$) is:

$$R_{\text{arm-x}}^\omega = R'_0 + \frac{R_{\text{AMR}}}{2} \cos 2\varphi_H. \quad (4)$$

By following the same derivations on arm-y, we can obtain the first harmonic resistance of arm-y ($R_{\text{arm-y}}^\omega$) as:

$$R_{\text{arm-y}}^\omega = R'_0 - \frac{R_{\text{AMR}}}{2} \cos 2\varphi_H, \quad (5)$$

Since R_{AMR} is much smaller than R_0 , we may write $R'_0 \approx R_0$. In the ideal case, when the four arms are identical, the first harmonic voltage of the bridge is given by

$$V_1^\omega = \frac{I_0}{2} (R_{arm-x}^\omega - R_{arm-y}^\omega) = V_{AMR} \cos 2\varphi_H, \quad (6)$$

where $V_{AMR} = \frac{I_0 R_{AMR}}{2}$ is the amplitude of V_1^ω . To account for the non-ideality of the device, we may write V_1^ω as

$$V_1^\omega = V_{AMR} \cos 2\varphi_H + C_{01}. \quad (7)$$

Here, C_{01} is the offset caused by misalignment or higher order angle-dependent terms due to inhomogeneous anisotropy in the sensing arms. The offset can be eliminated in the initial calibration process by subtracting half of the sum of the maximum and minimum values from V_1^ω , after which the signal can be normalized by dividing it with the amplitude, V_{AMR} .

Similarly, by substituting the expressions of ∇T , \vec{H}_{ext} , \vec{J}_x , \vec{m} into Equation (1), ignoring OMR and OHE, the transverse voltage on arm-x (V_2) can be expressed as:

$$V_2 = W \vec{E} \cdot \hat{y} = - \frac{WS_{ANE} K I_0^2}{8} \sin \theta_H \cos \varphi_H + \left(\frac{W \Delta \rho_{AMR} I_0}{4A} \sin^2 \theta_H \sin 2\varphi_H + \frac{W \rho_{AHE} I_0}{2A} \cos \theta_H \right) \sin \omega t + \frac{WS_{ANE} K I_0^2}{8} \sin \theta_H \cos \varphi_H \cos 2\omega t, \quad (8)$$

where W is the width of each arm, \hat{y} is a unit vector along y -axis. Here, $\frac{W \Delta \rho_{AMR} I_0}{4A}$ term corresponds to the contribution of planar Hall effect (PHE). When $\theta_H = 90^\circ$, $V_2^{2\omega}$ is:

$$V_2^{2\omega} = \frac{WS_{ANE} K I_0^2}{8} \cos \varphi_H = V_{ANE2} \cos \varphi_H, \quad (9)$$

where V_{ANE2} is the amplitude of $V_2^{2\omega}$. Using the same analysis method on arm-y, $V_3^{2\omega}$ is obtained as

$$V_3^{2\omega} = V_{ANE3} \sin \varphi_H, \quad (10)$$

where V_{ANE3} is the amplitude of $V_3^{2\omega}$. Considering the offsets, $V_2^{2\omega}$ and $V_3^{2\omega}$ may be written as:

$$V_2^{2\omega} = V_{ANE2} \cos \varphi_H + C_{02}, \quad (11)$$

$$V_3^{2\omega} = V_{ANE3} \sin \varphi_H + C_{03}, \quad (12)$$

where C_{02} and C_{03} are the transverse offset terms for the two arms, respectively. In practical situations, C_{02} and C_{03} can be ignored as they are very small.

3.2. Measured Angle Dependence of Harmonic Signals

Figure 2a shows the relationship between φ_H and V_1^ω , obtained from a Wheatstone bridge consisting of CoFeB (6 nm)/MgO (2 nm)/Ta (1.5 nm), from bottom to top. The AC current applied has an amplitude of 15 mA and frequency of 115 Hz. The in-plane field applied is 500 Oe, which is sufficient to saturate the magnetization into the field direction. The offset of V_1^ω has been subtracted from the raw data. The blue circle represents the measurement results, while the solid line depicts the fitting curves obtained using Equation (7). For this sample, the amplitude of V_1^ω is 21.5 mV and the offset is 14.9 mV. Figure 2b shows that the absolute error (ΔV) exhibits a $\cos 4\varphi_H$ dependence, which is presumably caused by the induced anisotropy introduced by the magnetic field applied during deposition, although its magnitude is very small [23,24], indicating that the output signal exhibits good agreement with the expected $\cos 2\varphi_H$ dependence.

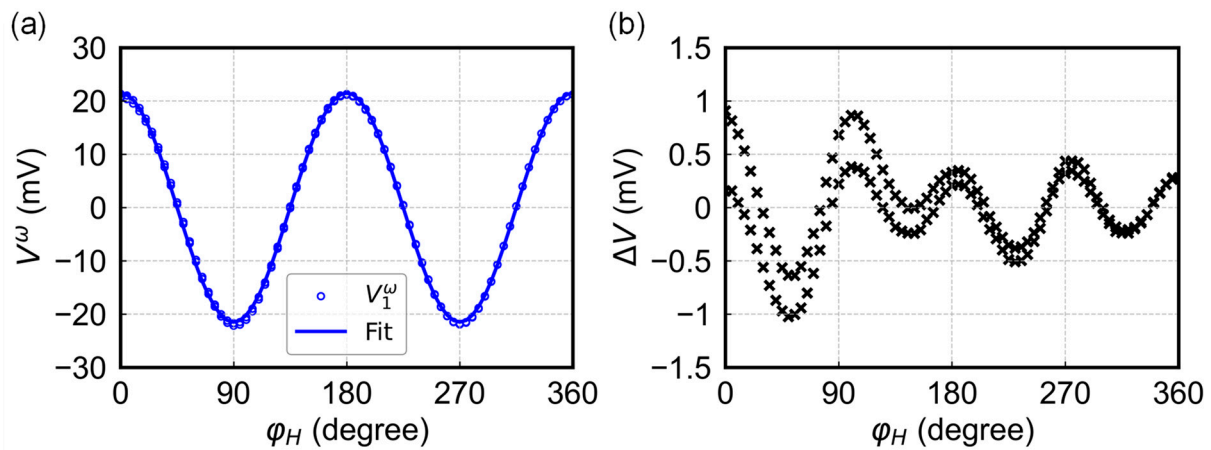


Figure 2. (a) Measured harmonic voltage V_1^ω (open circle), as a function of ϕ_H and its fitting curve (solid line). The offset has been subtracted from the raw data. (b) Absolute error distribution of V_1^ω as a function of ϕ_H .

Figure 3a shows the relationship between ϕ_H and $V_2^{2\omega}$ and $V_3^{2\omega}$, respectively, acquired under same conditions as that of V_1^ω . The solid green and orange lines represent the fitting curves obtained using Equations (11) and (12). The angle dependence of $V_2^{2\omega}$ and $V_3^{2\omega}$ closely aligns with the fitting curves, indicating high consistency with the cosine and sine angle dependence. The amplitudes of $V_2^{2\omega}$ and $V_3^{2\omega}$ are nearly the same at 10.6 μV . As shown in Figure 3b, the deviation from the ideal sine and cosine dependence is quite small compared to the measured signal, with an average magnitude of 0.12 μV and 0.14 μV , respectively, for $V_2^{2\omega}$ and $V_3^{2\omega}$. Judging from its angle dependence, it is probably caused by higher order harmonics due to the Oersted field [19,25], apart from the electronic noises.

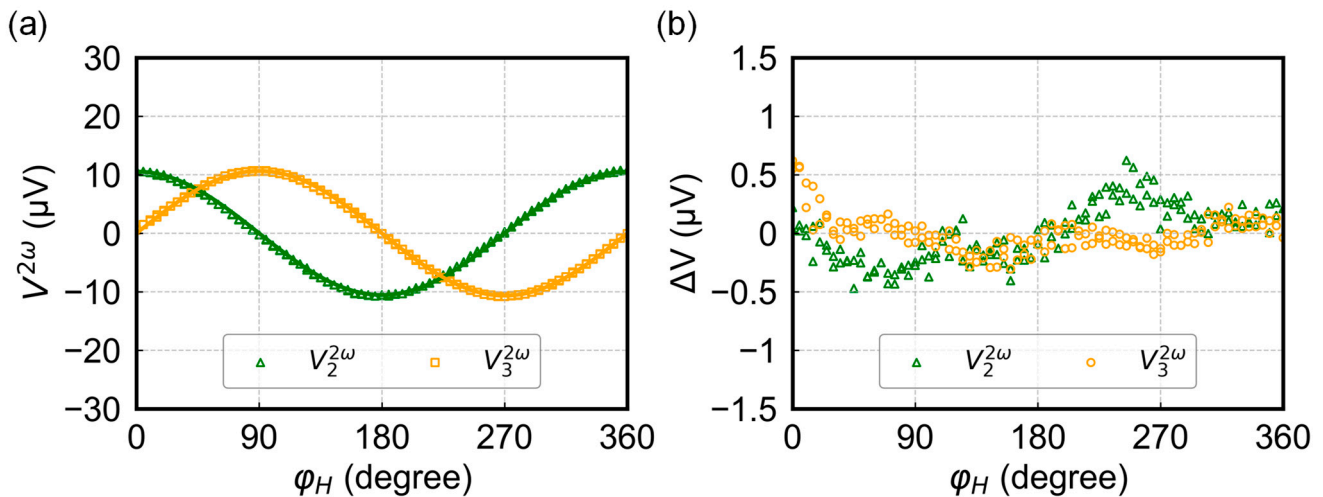


Figure 3. (a) Measured harmonic voltages $V_2^{2\omega}$ (open triangle) and $V_3^{2\omega}$ (open square) as a function of ϕ_H and their fitting curves (solid line). (b) Absolute error distribution of $V_2^{2\omega}$ and $V_3^{2\omega}$ as a function of ϕ_H .

3.3. Angle Calculation from Harmonic Signals

We now proceed to the calculation of angles using the harmonic signals. There are two possible ways to calculate the angles using the combination of first and second harmonic signals. Method 1 involves the use of the first harmonic signal to calculate the angles in each quadrant and then using the sign of the second harmonic signal to determine actual angles within 0–360°. As illustrated in Figure 4, the sign combination of $V_2^{2\omega}$ and $V_3^{2\omega}$ is unique in each quadrant: both are positive for the 1st quadrant and negative for the

3rd quadrant, and one is positive and the other is negative in the 2nd and 4th quadrant, respectively. The combination of arccosine values calculated from V_1^ω and the sign of $V_2^{2\omega}$ and $V_3^{2\omega}$ allows one to determine the angles within 0–360°. The specific calculation steps are as follows:

- (i) Calculate input values (α) for acos function from Equation (7): $\alpha = \frac{V_1^\omega - C_{01}}{V_{AMR}}$;
- (ii) Calculate φ' : $\varphi' = \frac{1}{2}\text{acos}(\alpha)$, $\varphi' \in (0^\circ, 90^\circ)$;
- (iii) Determine the actual angle (φ) according to the sign of $V_2^{2\omega}$ and $V_3^{2\omega}$:

$$\varphi = \begin{cases} \varphi' & V_2^{2\omega} > 0 \text{ and } V_3^{2\omega} > 0 \\ 180^\circ - \varphi' & V_2^{2\omega} < 0 \text{ and } V_3^{2\omega} > 0 \\ 180^\circ + \varphi' & V_2^{2\omega} < 0 \text{ and } V_3^{2\omega} < 0 \\ 360^\circ - \varphi' & V_2^{2\omega} > 0 \text{ and } V_3^{2\omega} < 0 \end{cases} \quad (13)$$

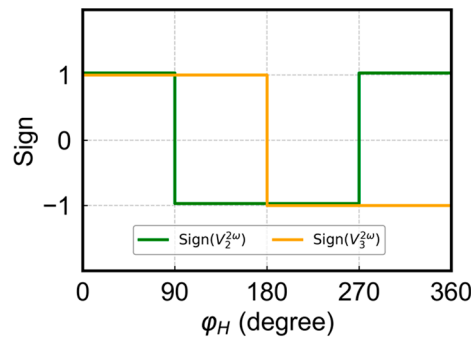


Figure 4. Sign of $V_2^{2\omega}$, $V_3^{2\omega}$.

The angle calculated from this method is, in general, quite accurate, except for the region near the maximum or minimum of $\cos 2\varphi$, due to the relatively slow change in these regions. Therefore, method 2 calculates the angle directly from $V_2^{2\omega}$ and $V_3^{2\omega}$ as follows:

$$\varphi = \text{atan2}\left(-\frac{V_3^{2\omega}}{V_{ANE3}}, -\frac{V_2^{2\omega}}{V_{ANE2}}\right) + \pi. \quad (14)$$

As is with method 1, φ calculated from $V_2^{2\omega}$ and $V_3^{2\omega}$ contains large errors near the maximum and minimum values of $\cos \varphi_H$ and $\sin \varphi_H$. Therefore, we combined the two methods by setting proper boundary values for the absolute value of α to divide them for use in different angle regions. By varying the boundary values between 0.8 and 0.99, we calculated the mean and maximum angle errors. The results indicated that when the boundary value is set between 0.86 and 0.9, both the mean and maximum angle errors reach their minimum values. Considering the larger amplitude of the first harmonic signal, we chose a larger value, 0.9, as the boundary value for distinguishing between the two calculation methods. When the absolute value of α was less than 0.9, we used method 1 to calculate the angles; when the absolute value of α was greater than 0.9, we employed method 2.

Figure 5a shows the relationship between the measured and actual field angles, showing a good agreement between the two in the entire angle range of 0–360°. The angle errors based on the combined method are shown in Figure 5b, with the angles around 0°, 90°, 180°, 270°, and 360° calculated by method 2 (with errors between 0° and 1.9°) and the rest by method 1 (with errors in the range of 0–1.5°). The mean error is 0.54°, which is comparable to commercial devices with multiple sensors. For comparison, the angular distributions of errors calculated separately using method 1 and method 2 are shown in Figure 5c,d, with mean angle errors of 0.85° and 0.67°, and maximum angle errors of 8.39° and 1.92°, respectively, which are much larger than those from the combined method. The large angle errors around 0°, 90°, 180°, 270°, and 360° in Figure 5c arise from the fact that

the noise affects the calculated values most in regions where cosine and sine functions are at the extrema points. Employing method 2 in these regions effectively reduces both the maximum and mean angle errors.

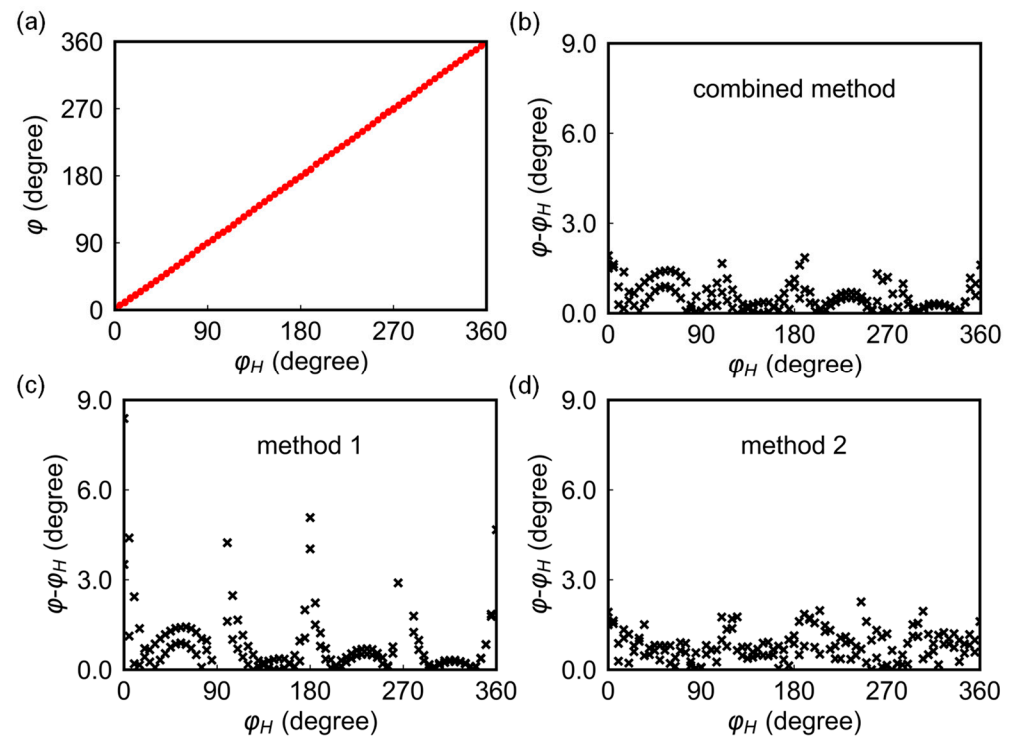


Figure 5. (a,b) Angle φ and angle error distribution as a function of φ_H using the combined method. (c,d) Angle error distribution using method 1 and method 2.

3.4. Performance Optimization

3.4.1. Effect of FM Layer Thickness

Figure 6 shows the amplitudes of V_1^ω (square) and $V_2^{2\omega}$ (circle) as a function of CoFeB thickness obtained with a fixed magnetic field strength of 500 Oe and the same dissipation power of 190 mW (by varying the current). The measurements were performed on samples of the following four different thicknesses: 3, 6, 10, and 15 nm. It is observed that, as the thickness increases, the amplitudes of both V_1^ω and $V_2^{2\omega}$ decrease. Consequently, thinner samples under the same power consumption condition result in a higher output voltage. However, it is important to note that at a thickness of 3 nm the sample is susceptible to over-heating due to high resistance. Therefore, a CoFeB thickness of 6 nm was chosen in this study.

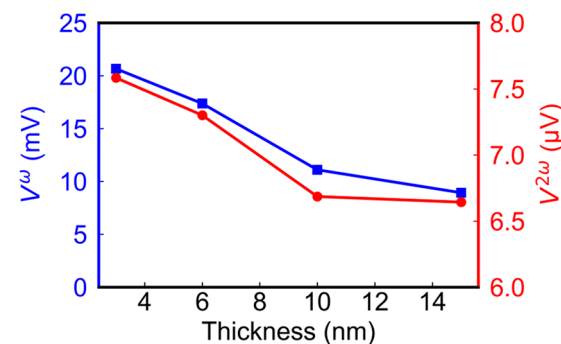


Figure 6. Relationship between the thickness of CoFeB and the amplitude of first (red circle) and second harmonic (blue square) signals.

3.4.2. Effects of Current Amplitude

After determining the thickness of the FM layer, we investigated the effect of current amplitude on the sensor output signals and angle errors. Figure 7a illustrates the mean angle error calculated with different current amplitudes using a 6 nm thick sensor. At low currents, the mean angle error is large, reaching approximately 14° . As the current amplitude increases to 15 mA and above, the mean angle error stabilizes at around 0.51° . The reason for this is that the fitting error of the output signals significantly affects the accuracy of angle calculation, as shown in Figure 7b. The blue and red solid lines depict the relationship between the fitting errors of the first and second harmonic signals with the current, respectively. Here, the fitting error is defined as $\frac{1}{N} \sum_{i=1}^N \frac{|\Delta V_i|}{V_{amp}}$, where V_{amp} is the amplitude of the first or second harmonic signals, ΔV_i is the difference between the measured and the fitted values at the i th measurement point, and N is total number of measurement points. At low currents, the fitting error of the second harmonic signal is more pronounced, reaching up to 30%, primarily due to the small temperature gradient. When the current exceeds 15 mA, the second harmonic signal's fitting error reaches a minimum. The inset in Figure 7b reflects the proportional relationship between the second harmonic signal and the square of the current amplitude, which is due to $\nabla T \propto I^2$, as mentioned above. On the other hand, the fitting error of the first harmonic signal remains relatively stable within the measurement current range. This stability is attributed to the effective compensation provided by the Wheatstone bridge structure, mitigating changes in resistance on different arms of the Wheatstone bridge caused by temperature rises. Taking energy efficiency into consideration, we set the current amplitude at the inflection point of the second harmonic signal's fitting error, i.e., 15 mA, as the input for the sensor.

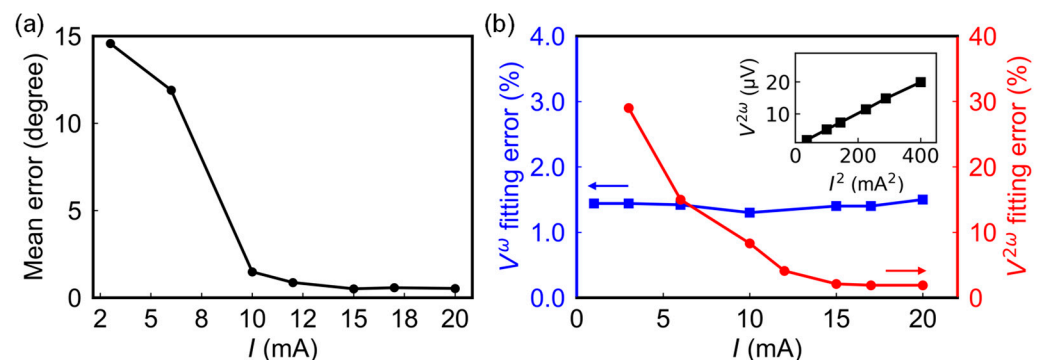


Figure 7. (a) Mean angle error calculated with different current amplitudes using a sensor with 6 nm CoFeB. (b) The relationship between current and fitting errors of the first (blue square) and second (red circle) harmonic signals. Inset shows the proportional relationship between the amplitude of second harmonic signal and I^2 .

3.5. Magnetic Field and Temperature Dependence

Harmonic voltages V_1^ω , $V_2^{2\omega}$, and $V_3^{3\omega}$ as a function of φ_H under a wide range of magnetic fields are shown in Figure 8a–c. The amplitude of the first and second harmonic signals are between 21.13–21.98 mV and 10.65–11.16 μV , respectively, within the 100–10,000 Oe range. The solid line in Figure 8d illustrates the output curve of a commercial Hall effect angle sensor, TMAG5170 [26] at 1500 Oe. When the external magnetic field is larger than 1000 Oe, which is the maximum detection field of the TMAG5170 sensor, it becomes ineffective, failing to produce an ideal sinusoidal or cosine curve, as per the dashed lines shown in Figure 8d. However, for our sensor, when the field is larger than 300 Oe, the curves overall remain at the same amplitude, indicating its weak dependence on the strength of the applied field. This can be advantageous in practical applications with a diverse field range.

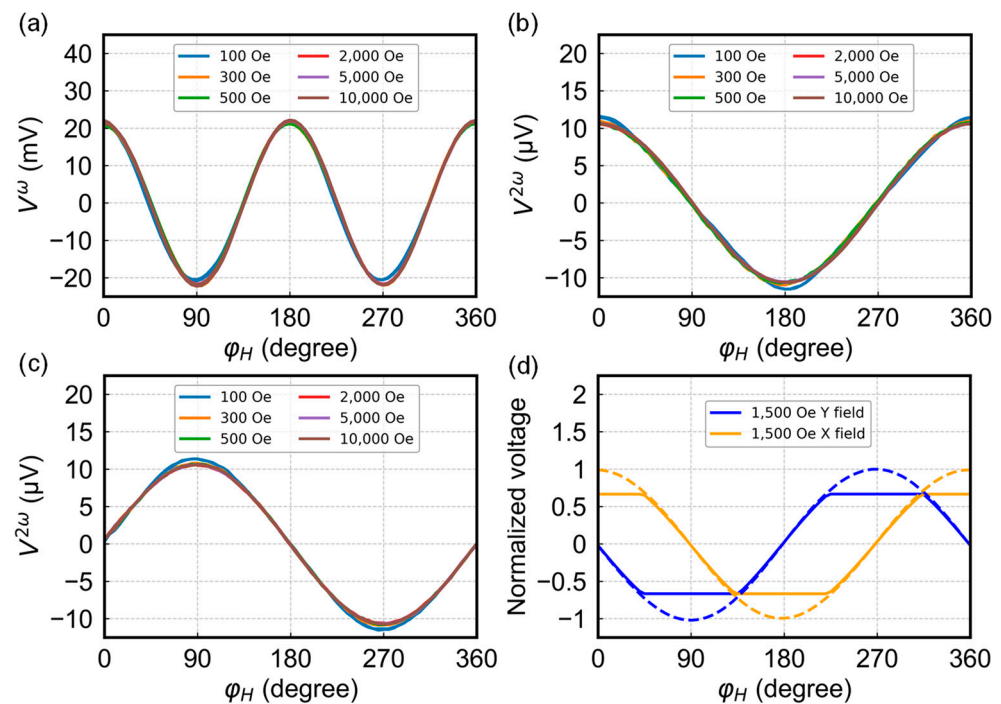


Figure 8. (a–c) Harmonic voltages V_1^ω , $V_2^{2\omega}$ and $V_3^{3\omega}$ as a function of ϕ_H under a wide range of magnetic fields. (d) Normalized voltage curves of TMAG5170 under 1500 Oe (solid lines). The dashed lines are ideal output curves when the field is within the detection range.

We use the same combined calculation method to calculate the angles under different external fields in the range of 100–10,000 Oe. As shown in Figure 9, overall, the mean and maximum angle errors exhibit very small variations at different magnetic fields. The mean angle error (red circle) fluctuates between 0.51° and 1.05° within the 100 Oe to 10,000 Oe range, reaching its minimum of around 0.51° between 500 Oe and 700 Oe, while the maximum angle error (blue square) ranges from 1.9° to 3.7° within the field range.

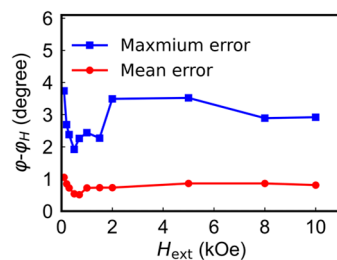


Figure 9. Mean and the maximum angle errors as a function of external field ranging from 100 to 10,000 Oe at 298 K.

Finally, we also investigated the temperature effect. As the temperature rises, the scattering dependent extrinsic contributions to AMR effect decrease [27], which results in the monotonic decrease of the first harmonic signal amplitude, ranging from 19.67 to 23.77 mV, with a change of 17.25% in the temperature range of 198 to 398 K (Figure 10a). Also shown in this figure is the temperature dependence of the second harmonic signal. Compared to the first harmonic signal, the relative decrease of the second harmonic signal is even larger, at about 23% from 198 K to 398 K. Apart from magnetic and electronic origins, the decrease in temperature gradient may also play a role as the increase in surrounding temperature may make it difficult for heat to diffuse and release through the substrate. The large decrease in second harmonic signals and the increase in thermal noise leads to large maximum angle errors, as shown in Figure 10b. Under the temperature range of 198–398 K

at 500 Oe, the mean angle error remains stable at $0.49\text{--}1.01^\circ$, while the maximum angle error increases in the range of $1.9\text{--}6.5^\circ$. This may pose challenges for the sensor's use at elevated temperatures. To enhance the signal stability of the sensor at high temperatures, it is crucial to have a well-designed heat flux path on the substrate or use a substrate with high thermal conductivity; this will be part of our future work. More systematic studies on the thermal engineering aspect are required in order to examine the suitability of the sensor for applications covering a wide temperature range from -100°C to 150°C , or even higher.

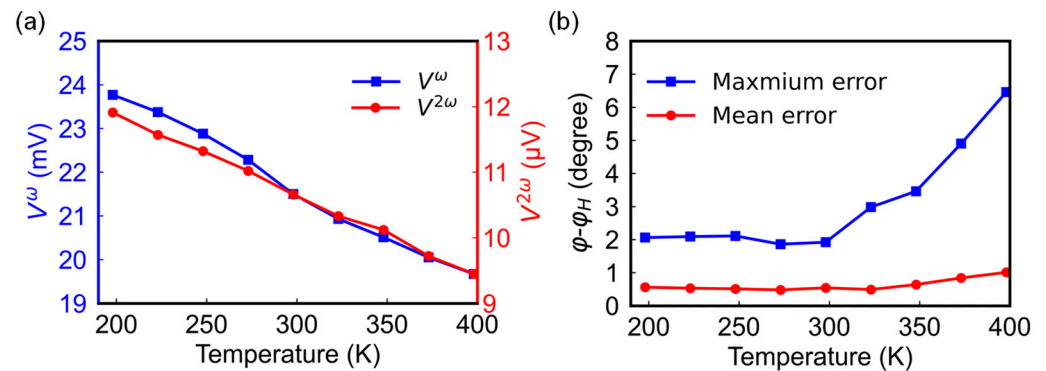


Figure 10. (a) First (blue square) and second (red circle) harmonic signal amplitudes as a function of temperature. (b) Mean and the maximum angle error within a temperature range of 198–398 K at a fixed field of 500 Oe.

4. Discussion

Compared to full 360° commercial magnetic position sensors and SOT-based angle sensors as shown in Table 1 [10,13,16,17,25], the sensor presented in this work exhibits several notable advantages, particularly in its structural simplicity. Utilizing a single Wheatstone bridge structure, our sensor distinguishes itself from other magnetic field sensors that often necessitate the combination of multiple devices. It is worth pointing out that most full-angle magnetic sensors utilize the atan2 function for angle calculation, whereas our approach primarily relies on the acos function. In comparison to the atan2 function, the acos function may introduce larger errors at certain angles due to its domain limitations. As a mitigation measure, at these points, we employed second harmonic signals as the inputs to atan2 function, overcoming the drawbacks of the acos function. This allowed us to achieve similar precision to commercially available magnetic angle sensors. Another key advantage is the stability of the signal across a wide magnetic field range (100–10,000 Oe). The absence of field-dependent components in the signal suggests that, in principle, the sensor can operate in a very large magnetic field. This unique property makes the sensor particularly well suited for diverse magnetic field applications. However, we also notice that at elevated temperatures, especially when surpassing 100°C , establishing a stable temperature gradient becomes challenging. The mean and maximum angle errors may increase at elevated temperature, which is currently the limitation of this type of sensor.

Table 1. Comparison of full 360° magnetic position sensors.

Model	Number of Devices	Dynamic Range (Oe)	Mean Error (Degree) ¹	Temperature Range ($^\circ\text{C}$)
TMR/GMR sensors [10]	2	300–500	0.7	$-40\text{--}150$
Hall effect sensors [25]	2	20–1000	0.4	$-40\text{--}150$
AMR sensors with GMR sensors [13]	3	200–600	0.1	$-40\text{--}125$
SOT vector magnetometer [16]	1	0–50	1.1	–
SOT-based sensor [17]	1	500–2000	0.4	–
AMR/ANE sensor in this study	1	>100	0.5	$-80\text{--}80$

¹ Only the mean errors within their optimal magnetic field ranges are listed here.

5. Conclusions

In conclusion, we have designed an alternative type of magnetic position sensor based on the ANE and AMR. It consists of a single Wheatstone bridge and can measure in-plane magnetic field angles within the full range of 0–360°. The combination of AMR and ANE signals reduces both mean and maximum angle errors. The prototype device exhibits a mean angle error of 0.51° at a field range of 500–700 Oe at room temperature, and further performance improvement and applicability expansion can be achieved through material and device geometry optimization. Considering its simple structure and suitability for wide magnetic field ranges, our design may present a cost-effective approach for magnetic position sensing.

Author Contributions: Y.W. conceived the idea and supervised the project. J.W. designed and fabricated the device and performed the measurements. J.W. and Y.W. analyzed the data. H.X. performed the experimental work of the project at the initial stage. J.W. and Y.W. wrote the manuscript. All authors have read and agreed to the published version of the manuscript.

Funding: This work is supported by the Advanced Research and Technology Innovation Centre (ARTIC), the National University of Singapore under Grant A-0005947-23-00, and NUS GAP Funding (RIE2025) under Grant A-8000656-00-00.

Institutional Review Board Statement: Not applicable.

Informed Consent Statement: Not applicable.

Data Availability Statement: Data are contained within the article.

Conflicts of Interest: The authors declare no conflicts of interest.

References

1. Wu, J.; Hu, Z.; Gao, X.; Cheng, M.; Zhao, X.; Su, W.; Wang, Z.; Zhou, Z.; Dong, S.; Liu, M. A Magnetoelectric Compass for In-Plane AC Magnetic Field Detection. *IEEE Trans. Ind. Electron.* **2020**, *68*, 3527–3536. [CrossRef]
2. Hahn, R.; Schmidt, T.; Seifart, K.; Oiberts, B.; Romera, F. Development of a magneto-resistive angular position sensor for space mechanisms. In Proceedings of the 43rd Aerospace Mechanisms Symposium, Santa Clara, CA, USA, 5 May 2016.
3. Kumar, A.A.S.; George, B.; Mukhopadhyay, S.C. Technologies and applications of angle sensors: A review. *IEEE Sens. J.* **2020**, *21*, 7195–7206. [CrossRef]
4. Hu, G.; Jiang, J.; Lee, K. Parametric and Noise Effects on Magnetic Sensing System for Monitoring Human-Joint Motion of Lower Extremity in Sagittal Plane. *IEEE Sens. J.* **2023**, *23*, 4729–4739. [CrossRef]
5. Bermúdez, C.; Santiago, G.; Fuchs, H.; Bischoff, L.; Fassbender, J.; Makarov, D. Electronic-skin compasses for geomagnetic field-driven artificial magnetoreception and interactive electronics. *Nat. Electron.* **2018**, *1*, 589–595. [CrossRef]
6. Sreevidya, P.V.; Khan, J.; Barshilia, H.C.; Ananda, C.M.; Chowdhury, P. Development of two axes magnetometer for navigation applications. *J. Magn. Magn. Mater.* **2018**, *448*, 298–302. [CrossRef]
7. Malinowski, G.; Hehn, M.; Montaigne, F.; Schuhl, A.; Duret, C.; Nantua, R.; Chaumontet, G. Angular magnetic field sensor for automotive applications based on magnetic tunnel junctions using a current loop layout configuration. *Sen. Actuators A* **2008**, *144*, 263–266. [CrossRef]
8. Hall Effect Position Sensor, 103RS Datasheet, Honeywell. Available online: <https://prod-edam.honeywell.com/content/dam/honeywell-edam/sps/siot/ja/products/sensors/magnetic-sensors/value-added-packaged-sensors/103sr-series/documents/sps-siot-103sr-series-hall-effect-position-sensor-sealed-housing-product-sheet-005971-1-en-ciid-150029.pdf> (accessed on 19 December 2023).
9. AMR Sensors, ADA4571 Datasheet, Analog Device. Available online: <https://www.mouser.sg/datasheet/2/609/ADA4571-3120436.pdf> (accessed on 19 December 2023).
10. GMR Angle Sensor, TLE5011 Datasheet, Infineon. Available online: https://www.infineon.com/dgdl/Infineon-TLE5011-DataSheet-v02_00-en.pdf?fileId=db3a30432ee77f32012f0c4368b5110e (accessed on 19 December 2023).
11. Giebler, C.; Adelerhof, D.J.; Kuiper, A.E.T.; van Zon, J.B.A.; Oelgeschlager, D.; Schulz, G. Robust GMR sensors for angle detection and rotation speed sensing. *Sen. Actuators A* **2001**, *91*, 16–20. [CrossRef]
12. Dimitrova, P.; Andreev, S.; Popova, L. Thin film integrated AMR sensor for linear position measurements. *Sen. Actuators A* **2008**, *147*, 387–390. [CrossRef]
13. AMR/GMR Angle Sensor, TLE5x09A16 Datasheet, Infineon. Available online: https://www.infineon.com/dgdl/Infineon-TLE5x09A16_D-DataSheet-v02_00-EN.pdf?fileId=5546d462696dbf12016977889fe858c9 (accessed on 19 December 2023).
14. Xu, Y.; Yang, Y.; Zhang, M.; Luo, Z.; Wu, Y. Ultrathin All-in-One Spin Hall Magnetic Sensor with Built-In AC Excitation Enabled by Spin Current. *Adv. Mater. Technol.* **2018**, *3*, 1800073. [CrossRef]

15. Xie, H.; Chen, X.; Luo, Z.; Wu, Y. Spin torque gate magnetic field sensor. *Phy. Rev. Appl.* **2021**, *15*, 024041. [[CrossRef](#)]
16. Chen, X.; Xie, H.; Shen, H.; Wu, Y. Vector Magnetometer Based on a Single Spin-Orbit-Torque Anomalous-Hall Device. *Phy. Rev. Appl.* **2022**, *18*, 024010. [[CrossRef](#)]
17. Luo, Z.; Xu, Y.; Yang, Y.; Wu, Y. Magnetic angular position sensor enabled by spin-orbit torque. *Appl. Phys. Lett.* **2018**, *112*, 262405. [[CrossRef](#)]
18. Shiogai, J.; Fujiwara, K.; Nojima, T.; Tsukazaki, A. Three-dimensional sensing of the magnetic-field vector by a compact planar-type Hall device. *Commun. Mater.* **2021**, *2*, 102. [[CrossRef](#)]
19. Avci, C.O.; Garelo, K.; Gabureac, M.; Ghosh, A.; Fuhrer, A.; Alvarado, S.F.; Gambardella, P. Interplay of spin-orbit torque and thermoelectric effects in ferromagnet/normal-metal bilayers. *Phys. Rev. B* **2014**, *90*, 224427. [[CrossRef](#)]
20. Chen, Y.; Roy, D.; Cogulu, E.; Chang, H.; Wu, M.; Kent, A.D. First harmonic measurements of the spin Seebeck effect. *Appl. Phys. Lett.* **2018**, *113*, 202403. [[CrossRef](#)]
21. Uchida, K.; Kikkawa, T.; Seki, T.; Oyake, T.; Shiomi, J.; Qiu, Z.; Takanashi, K.; Saitoh, E. Enhancement of anomalous Nernst effects in metallic multilayers free from proximity-induced magnetism. *Phys. Rev. B* **2015**, *92*, 094414. [[CrossRef](#)]
22. Harder, M.; Gui, Y.; Hu, C.M. Electrical detection of magnetization dynamics via spin rectification effects. *Phys. Rep.* **2016**, *661*, 1–59. [[CrossRef](#)]
23. Guo, Y.; Yong, D.; Wang, S.X. Multilayer anisotropic magnetoresistive angle sensor. *Sen. Actuators A* **2017**, *263*, 159–165. [[CrossRef](#)]
24. Sreevidya, P.V.; Borole, U.P.; Kadam, R.; Khan, J.; Barshilia, H.C.; Chowdhury, P. A novel AMR based angle sensor with reduced harmonic errors for automotive applications. *Sen. Actuators A* **2021**, *324*, 112573.
25. Shao, Q.; Yu, G.; Lan, Y.W.; Shi, Y.; Li, M.Y.; Zheng, C.; Zhu, X.; Li, L.J.; Amiri, P.K.; Wang, K.L. Strong Rashba-Edelstein Effect-Induced Spin-Orbit Torques in Monolayer Transition Metal Dichalcogenide/Ferromagnet Bilayers. *Nano Lett.* **2016**, *16*, 7514–7520. [[CrossRef](#)]
26. 3D Linear Hall-Effect Sensor, TMAG5170 Datasheet, Texas Instruments. Available online: <https://www.ti.com/lit/ds/symlink/tmag5170-q1.pdf?ts=1702977310932> (accessed on 19 December 2023).
27. Park, J.H.; Ko, H.W.; Kim, J.M.; Park, J.; Park, S.Y.; Jo, Y.; Park, B.G.; Kim, S.K.; Lee, K.J.; Kim, K.J. Temperature dependence of intrinsic and extrinsic contributions to anisotropic magnetoresistance. *Sci. Rep.* **2021**, *11*, 20884. [[CrossRef](#)] [[PubMed](#)]

Disclaimer/Publisher’s Note: The statements, opinions and data contained in all publications are solely those of the individual author(s) and contributor(s) and not of MDPI and/or the editor(s). MDPI and/or the editor(s) disclaim responsibility for any injury to people or property resulting from any ideas, methods, instructions or products referred to in the content.